

# Polar maps of C-band backscatter parameters from the Advanced Scatterometer

Jessica Cartwright<sup>1,2,3†</sup>, Alexander D. Fraser<sup>4,5,3</sup>, Richard Porter-Smith<sup>4</sup>

<sup>1</sup>National Oceanography Centre, European Way, Southampton, SO14 3ZH, UK

5 <sup>2</sup>Ocean and Earth Science, National Oceanography Centre Southampton, University of Southampton, Southampton, SO14 3ZH, UK

<sup>3</sup>Antarctic Climate & Ecosystems Cooperative Research Centre, University of Tasmania, Private Bag 80, Hobart, Tasmania 7001, Australia

10 <sup>4</sup>Australian Antarctic Program Partnership, Institute for Marine and Antarctic Studies, University of Tasmania, Hobart, Tasmania, Australia

<sup>5</sup>Institute for Marine and Antarctic Studies, University of Tasmania, Hobart, Tasmania, Australia

*Correspondence to:* Jessica Cartwright (jessica.cartwright@spire.com)

**Abstract.** Maps of backscatter anisotropy parameters from the European Organisation for the Exploitation of Meteorological  
15 Satellites (EUMETSAT) Advanced Scatterometer (ASCAT), a C-band fan-beam scatterometer, contain unique and valuable  
data characterising the surface and subsurface of various cryospheric elements, including sea ice and ice sheets. The  
computational expense and considerable complexity required to produce parameter maps from the raw backscatter data inhibits  
the wider adoption of ASCAT data. Here, backscatter anisotropy parameter maps gridded at a resolution of 12.5 km per pixel  
are made available to the community in order to facilitate the exploitation of these parameters for cryospheric applications.  
20 These maps have been calculated from the EUMETSAT Level 1B sigma0 product acquired from ASCAT on board MetOp-  
A, MetOp-B and MetOp-C. The dataset is unique in that it prioritises anisotropy characterisation over temporal resolution, and  
combines ASCAT data from multiple platforms. The parameterisation chosen assumes a linear falloff of backscatter with  
incidence angle and a 4th order Fourier series parameterisation of azimuth angle anisotropy. The product (Fraser and  
Cartwright, 2021) is available at <https://doi.org/10.26179/5dd60df7469e2> presented on three time scales depending on orbital  
25 platform availability: 5-day (2007 to 2020 – MetOp-A only – suitable for users requiring a long time-series), 2-day (2013 to  
2020 – MetOp-A and -B), and 1-day resolution (2019 – 2020 – MetOp -A, -B and -C – suitable for users needing both high  
temporal resolution and detailed anisotropy characterisation). Datasets will be updated annually.

## 1 Introduction

30 Observation and characterisation of the polar cryosphere is of critical importance in understanding changes to the Earth's  
climate system. The extent, variability and physical characteristics of snow and ice (and their trends), both grounded and

---

† Current Address: Spire Global Inc., Glasgow, UK

floating, have far-reaching climatic consequences, and can respond relatively rapidly to changes in atmospheric and oceanic forcing (Pörtner et al., 2019). Baseline characterisation of the physical properties of sea ice is increasingly important due to the recognition of the wide roles it plays in the physics of the Earth's climate, e.g. through the modification of the surface albedo (Stroeve et al., 2011), and its impact on the ocean circulation and weather (Comiso et al., 2003). From a human perspective, there is also great interest in understanding Arctic sea ice for oil and gas exploitation and shipping routes (Bird et al., 2008). The Greenland Ice Sheet and parts of the Antarctic Ice Sheet are also undergoing profound changes in response to atmospheric and oceanic forcing, in the form of enhanced melt (both supra-glacial and sub-glacial in ice shelf cavities), resulting in mass loss and contributions to sea level rise (Holland et al., 2019; Shepherd et al., 2020).

The extent and remoteness of the polar cryosphere means that effective hemispheric, repeat monitoring and characterisation of these cryospheric elements can be provided only by spaceborne sensors. The cryosphere is currently observed by a range of spaceborne active and passive sensors, and across a wide swath of the electromagnetic spectrum (Lubin and Massom, 2006; Massom and Lubin, 2005). Each part of the spectrum is associated with a unique set of characteristics (e.g., ground resolution, cloud penetration, ice/snow penetration, response to ice properties, ease of interpretation). Here we draw attention to the useful physical characteristics which can be retrieved by non-nadir C-band (~5 GHz) radar backscatter cross-section (hereafter simply “backscatter”) in order to provide context for the interpretation of the dataset accompanying this paper.

## 2 C-band backscatter

The interaction of incident C-band radiation with a target (including both surfaces and subsurface volumes) depends on both the dielectric properties and physical structure of the target. In addition, depending on the physical properties of the target, C-band backscatter can exhibit strong anisotropy (i.e., as observation geometry-dependent measure of backscatter). This can manifest as anisotropy as a function of incidence angle, azimuth angle, or both, depending on the properties of the target. If the processes governing the anisotropy are well-understood, characterisation of this anisotropy can inform on the nature of the target. A further motivation for fully characterising the anisotropy is the removal of elements of the anisotropy, to retrieve an estimate of backscatter “uncontaminated” by those elements of anisotropy.

A wide variety of parameterisations of the microwave backscatter anisotropy from the Antarctic continent are reviewed in Fraser et al. (2014). To briefly summarise, incidence angle anisotropy at intermediate incidence angle ranges used by scatterometers (e.g., ~25 to 65 degrees) is widely modelled as a linear change with respect to incidence angle. Azimuthal anisotropy arises primarily due to the interaction between the incident microwave radiation and regularly aligned roughness (on the Rayleigh roughness scale, or larger) of the surface and subsurfaces within the penetration depth (Ulaby et al., 1996; Bingham and Drinkwater, 2000; Partington and Flach, 2003; Yurchak, 2009; Fraser et al., 2016). Where incident microwaves are perpendicular to this structured roughness, higher backscatter results. Such structured alignment is commonly encountered in sand dune systems, croplands (Bartalis et al., 2006) and over the Greenland and Antarctic ice sheets, in the form of sastrugi (Long and Drinkwater, 2000). This relationship is exploited over oceans, where ocean capillary wave properties (height and

alignment) are a function of the near-surface wind field. Scatterometer-based remote retrieval of azimuthal anisotropy over oceans, with real-time data from sensors such as ASCAT is thought to have increased weather forecast accuracies by as much as 30% through the monitoring of near-surface winds over the ocean (Figa-Saldaña et al., 2002).

## 2.1 Applications of Scatterometry to the Cryosphere

The following section provides a brief overview of interpreting backscatter anisotropy of the polar cryosphere (including sea ice and glacial ice sheets). For further information, the readers are referred to in-depth reviews of the topic provided by Long (2017) and Alley (2017). Here, we aim for a broad overview with sufficient context to understand the ASCAT-based dataset accompanying this paper.

Backscatter and anisotropy vary greatly between glacial ice, sea ice, dry snow and moisture-laden snow on sea ice, but also more subtly within each of these surface types. A primary signal characteristic to consider is the penetration depth of the signal into the medium. This determines whether the received signal is dominated by volume or surface scattering. For dry snow and glacial ice, C-band penetration depths can reach 20m or even more (Rignot et al., 2001; Müller et al., 2010), meaning backscatter has a considerable contribution from both internal layers of varying structure and density (surface scattering), as well as considerable volume backscatter. This penetration depth combined with the similar dielectric properties of air and dry snow mean that in smoother regions of the Antarctic continent, the majority of signal received can be from volume rather than surface scattering (Rott et al., 1993; Drinkwater et al., 2001). This allows for C-band incidence angle anisotropy to be effective for surface mass balance retrieval, via sensitivity to both snow grain size and the presence of dielectric layering, both of which are modified by the magnitude of the surface mass balance (Mätzler and Hüppi, 1989; Drinkwater et al., 2001).

Surface contributions (including those from buried surfaces such as sastrugi) are highly dependent on surface orientation and slope, Rayleigh scale roughness, and roughness anisotropy (Ashcraft and Long, 2007); enabling facies determination and sastrugi property retrieval (Remy et al., 1992; Ledroit et al., 1993). Surface scattering tends to dominate where penetration depth is minimal, such as over sea ice, yielding information on the degree of deformation of the ice itself. Backscatter is also greatly reduced by the incorporation of liquid water within the scattering volume (Trusel et al., 2012; Alley et al., 2018). Data collected during the sea ice melt season or areas of ice sheet experiencing melt must therefore be treated appropriately.

Icebergs are easily identifiable with simple thresholding techniques through their very high backscatter signatures (due to melt and refreeze) in comparison with the lower backscatter of sea ice (Young and Hyland, 1997; Budge and Long, 2018). Such studies are limited by the relatively low resolution of scatterometers; moderate-sized icebergs (up to ~2 km) are generally sub-pixel at the resolution of scatterometer datasets. Where higher resolution microwave backscatter data are required for iceberg discrimination, it is generally necessary to use spaceborne synthetic aperture radar (SAR) instruments (Young and Hyland, 1997; Budge and Long, 2018), however larger icebergs may be resolved in scatterometer data with the use of resolution enhancement techniques, e.g., Long et al. (1993).

## 2.2 C-band sensors

95 There are three classes of active instrument using C-band: SAR, altimeters and scatterometers. SAR allows the collection of extremely high resolution imagery of the surface through the artificial extension of the antenna by the motion of the radar itself. This creates a very high data volume over a narrow swath, which is typically unsuitable for application over large areas. The data also provide minimal incidence and azimuth angle diversity, precluding characterisation of the microwave backscatter anisotropy detailed above. Altimeters measure backscatter at a nadir (or near-nadir) incidence angle, again providing no  
100 diversity of incidence/azimuth angle and precluding characterisation of anisotropy.

Scatterometers enable the collection of radar backscatter data at a variety of azimuth angles but at relatively low spatial resolution compared to SAR. Compared to SAR, scatterometers are generally better suited to large-scale studies, with a spatial resolution of typically ~30 km, but potential for below 10 km (Long et al., 1993). These sensors take two main forms — a rotating pencil-beam, such as SeaWinds (Spencer et al., 1997) and a sweeping fan beam (e.g. SeaSat Scatterometer, NASA  
105 Scatterometer, European Remote Sensing Satellite-1 or Advanced Scatterometer). In the case of pencil beam scatterometry, the diversity of azimuth angle measurements comes from the (azimuthal) rotation of the antenna. As such, pencil-beam scatterometers are typically limited in incidence angle diversity. Fan-beam scatterometers use multiple fixed antennae at different orientations allowing multiple looks at each pixel in a swath-like signal. This configuration combined with the spacecraft orbit means that over a given time interval, backscatter from a point on the surface is measured from a wide variety  
110 of both incidence (~25 to 65 degrees for ASCAT) and azimuth angles (azimuth range dependent on latitude of observation, see Fraser et al. (2014)).

The processing of scatterometer data is highly computationally expensive due to the large quantities of data involved and processing time required for multivariate parameter estimation. Choice of parameterisation model is not straight-forward, with a wide variety covered by Fraser et al. (2014), however this dataset aims to make scatterometry data more accessible to the  
115 cryosphere research community through the computation of broadly-applicable parameters over both polar areas using an anisotropy model with proven applications in cryospheric remote sensing (Fraser et al., 2014; Fraser et al., 2016). It is anticipated that the provision of this dataset will enable the increased exploitation of scatterometry for cryosphere research purposes over a variety of time scales at as high a temporal resolution as possible, whilst retaining 100% coverage at 5- and 2-day timescales and >92% coverage at daily resolution.

## 120 2.3 Previous similar datasets

Several ASCAT-based backscatter datasets exist, but are either:

- a) low-level unprocessed data — i.e., anisotropy-affected raw backscattering cross section measurements, such as the source data used here;

- b) based on simple anisotropy parameterisations and containing unaccounted-for azimuthal anisotropy — for example products distributed by the Centre de Recherche et d’Exploitation Satellitaire (CERSAT) and the National Aeronautics and Space Administration Scatterometer Climate Record Pathfinder Project (NASA SCP);
- c) highly processed end-product datasets representing retrieved physical quantities — e.g., sea ice extent, Arctic sea ice type, ocean wind and soil moisture parameters, etc. (OSI SAF, 2019a, b).

Our dataset (shown in Figure 1 and Figure 2) represents a balance between these product types, providing the computationally-expensive parameter calculation whilst making minimal assumptions regarding the physical meaning of the parameters presented and accounting for anisotropy from both incidence and azimuth angles. It is anticipated that this dataset will facilitate exploitation of ASCAT data for cryospheric parameter retrieval.

The datasets described in b) (CERSAT and NASA SCP) represent those most closely comparable with that presented here. Key differences between this dataset and those readily available stem from the more complex and computationally expensive parameterisation required to account for the azimuthal anisotropy in the backscatter measurements (seen in Figure 3). A trade-off we make in performing a detailed anisotropy characterisation is the preclusion of parameter retrieval in regions with a limited number of observations. We retrieve a total of 8 parameters, so require at least 8 observations of the surface for parameter estimation to occur. This, in turn, requires at least three ASCAT passes (each pass gives three unique observations). Products normalising only by incidence angle (e.g. CERSAT and NASA SCP) require only one pass to provide sufficient observations, yielding marginally higher coverage at latitudes further from the geographical pole (Figure 4) and due to this an increased return rate. Figure 5 shows a direct comparison of the datasets averaged over the entirety of 2017, with both datasets gridded to the same spatial resolution. A and B parameter difference maps shown in Figure 5c) and d), respectively, indicate that the two products partition backscatter differently between these two parameters, with regions of positive A parameter difference coinciding with negative B parameter difference, and vice versa. Figure 5f) also shows the high to low azimuthal diversity zones clearly as a discontinuity in the B parameter in the SCP product, indicating that the more sophisticated parameterisation presented here handles this viewing geometry regime change more seamlessly.

Data from ASCAT are currently used for the characterisation of global sea ice extent, as well as ice type retrieval in the Northern Hemisphere (Breivik et al., 2012). These products are routinely produced, and available from Ocean and Sea Ice Satellite Application Facility (OSI SAF — [www.osi-saf.org](http://www.osi-saf.org)). Ice extent calculations exploit the difference in backscatter received by the fore and rear antennas in combination with passive microwave sensors. A Bayesian methodology is applied with the use of training areas to identify sea ice, open water, and in the Northern Hemisphere, sea ice type (Breivik et al., 2012). Similar parameters to those used by OSI SAF for the creation of these Level 2 products may be extracted from the more comprehensive parameterisation presented here, demonstrating their use in the classification of ice surfaces and allowing these same techniques to be applied over a wider variety of applications in the cryosphere

We note that spatial resolution-enhanced ASCAT products exist (Long et al., 1993; Vogelzang and Stoffelen, 2017) but emphasise that the present dataset focusses not on resolution but a relatively detailed parameterisation (to ensure minimal residual anisotropy), and parameter estimation with the shortest possible time interval, which is determined by the number of

MetOp platforms operational at the time. In future work we hope to combine all three attributes for enhanced spatial resolution, complex parameterisation and high temporal resolution.

### 160 3 ASCAT and Metop-A, -B and -C platforms

The backscatter data used in this study are acquired from the Advanced SCATterometer (ASCAT) onboard Metop-A, -B and -C. These three satellites have been put into orbit at an inclination of  $98.2^\circ$  and an altitude of 817 km into sun-synchronous orbits with a period of 101 minutes (Figa-Saldaña et al., 2002). Each satellite has a 29-day repeat cycle, and a 5-day subcycle. The launch dates and data availability of each of the three satellites can be seen in Table 1 below, with the overlapping periods of data availability enabling a reduction in parameter map time-step from 5-day maps before 2013 (only MetOp-A), to 2-day maps (MetOp-A and -B), and daily resolution as data become available from MetOp-C. MetOp-B and -C are in the same plane, spaced approximately half an orbit apart. Thus, with this pair alone, the orbital period is effectively reduced to 50 minutes. MetOp-A shares its period and inclination with -B and -C but has been drifting since 2017 to facilitate extension of its lifetime. It is now in a different plane but still providing high-quality backscatter measurements. The tri-platform observation network is projected to be operational until 2022.

**Table 1: Launch dates of MetOp-A, MetOp-B and MetOp-C and data availability from each.**

Platform	Launched	Data Available	Data Used
MetOp-A	October 2006	March 2007 – Present;	2008 - Present
MetOp-B	September 2012	December 2012 – Present	2013 - Present
MetOp-C	November 2018	June 2019 – Present	June 2019 - Present

ASCAT is a C-band (5.255 GHz) VV-polarisation scatterometer with six fan-beam antennas (Table 2). The antennas give a two-swath configuration, each approximately 550 km wide, with a 720 km sub-satellite gap, measuring backscatter up to  $88^\circ$  N/S. Three antenna pairs on each side ( $\pm 45^\circ$ ,  $\pm 90^\circ$  and  $\pm 135^\circ$  of azimuth relative to the sub-satellite track) give a wide variety of azimuth and incidence angles ( $25\text{-}65^\circ$ ), seen in Figure 3. Over a 5-day subcycle, these provide many looks of a region of the Earth’s surface with a high diversity of both incidence and azimuth angles (Fraser et al., 2014). The current half-orbit (50 minute) spacing of MetOp-B and -C gives highly complementary coverage of polar regions: i.e., a 50 minute interval corresponds to an Earth rotation of 12.5 degrees. At a latitude of  $65^\circ$  (N or S), a 12.5 degree rotation corresponds to a distance of  $\sim 580$  km, thus at this latitude, MetOp-B and -C observe within each other’s sub-satellite gap during subsequent passes. As MetOp-A’s orbit is drifting, this increases the diversity of observations and allows daily maps of the parameters given here, although the phasing of the orbit (and hence the degree to which it can be considered complementary) will drift over time.

**Table 2: Instrument and platform specifications**

	ASCAT		Metop-A	Metop-B	Metop-C
Frequency	C-band (5.255 GHz)	Period	101.3 mins	101.3 mins	101 mins
Beam configuration	3 antennas at 45, 90 and 135 degrees of azimuth on each side	Inclination	98.7°	98.7°	98.7°
Footprint	30 km x 10 km	Altitude	827 km	827 km	817 km
Swath Width	550 km	Mass	4085 kg	4087 kg	3950 kg
Sub-satellite gap	700 km	Power	1810 W	2210 W	2100 W

185

#### 4 Methods

Data were acquired in NetCDF format from the EUMETSAT Data Centre (“ASCAT GDS Level 1 Sigma0 resampled at 12.5 km Swath Grid — Metop”), data code ASCSZR1B. The 12.5 km resampled product is used here. The processing required to reach the resampled product results in a true spatial resolution of 25–30 km, as the full resolution product is smoothed in both the across- and along- track directions for gridding. There are approximately 14 complete-orbit files per day, starting and ending near the North Pole. These files contain geographic location data for each pixel, as well as azimuth, incidence,  $\sigma_0$  (Normalised Radar Cross Section or NRCS – here termed backscatter) and  $K_p$  (Residual Mean Square of the NRCS) values in the format of triplets (fore, mid and aft antennas), each with 82 data points per row.

The ASCAT swath data are then resampled onto the NSIDC polar stereographic 12.5 km grid, EPSG 3411 and 3412 for Northern and Southern Hemisphere respectively. This is performed separately for the northern and southern hemisphere data, with true latitude at 70° for each hemisphere. This grid was chosen in order to ensure wide availability of compatibility of other sea ice datasets, as well as ensuring minimal distortion of the grid in the sea ice region. This grid is 608 x 896 pixels in the northern hemisphere and 632 x 664 pixels in the southern hemisphere.

In regions exhibiting backscatter anisotropy, backscatter varies with incidence and azimuth angle, and such anisotropy needs to be characterised before physical parameter retrieval can take place. Accurate quantification of the anisotropy is undertaken by defining a model which describes the relationship between backscatter and the incidence/azimuth angles. Fraser et al. (2014) showed that a parameterisation featuring a linear falloff of incidence angle with increasing backscatter, plus a 1<sup>st</sup>, 2<sup>nd</sup> and 4<sup>th</sup> harmonic sinusoidal azimuthal response was a good choice for representing the anisotropy found on most of the Antarctic Ice Sheet. While work on sea ice parameter retrieval is still at a nascent stage, this same parameterisation shows promise in this domain too. Thus, we adopt parameterisation “Linear\_124” from Fraser et al. (2014) as a general parameterisation with a wide range of potential applications to the cryosphere. This is in contrast to other products mentioned above, modelling backscatter solely as a function of incidence angle and presents the relationship between these as a surface as a function of the two,  $\sigma_0 =$

$A + f(\theta) + g(\varphi)$  where  $\sigma_0$  represents the measured backscatter,  $\theta$  is the incidence angle and  $\varphi$  the azimuth angle of the observation. The "Linear\_124" from Fraser et al. (2014) is given in Equation (I) below.

$$\sigma_0 = A + B(\theta - 40^\circ) + m_1 \cos(1(\varphi - \varphi_1)) + m_2 \cos(2(\varphi - \varphi_2)) + m_4 \cos(4(\varphi - \varphi_4)) \quad (1)$$

210

Parameterisation is performed separately for the gridded data in the northern and southern hemispheres, and on three different timescales — every 5 days (using data from MetOp-A only), every 2-days (MetOp-A and -B) and daily parameter maps (data from MetOp-A, -B and -C). These parameters are detailed below and can be seen in Figure 1 and Figure 2:

- $A$  — Isotropic component of backscatter (normalised to a mid-range incidence angle of  $40^\circ$ )
- $B$  — Co-efficient describing the linear falloff of backscatter with increasing incidence angle
- $m_1$  and  $\varphi_1$  — Amplitude and phase of fundamental azimuth anisotropy component
- $m_2$  and  $\varphi_2$  — Amplitude and phase of bisinusoidal azimuth anisotropy component
- $m_4$  and  $\varphi_4$  — Amplitude and phase of 4th harmonic azimuth anisotropy component
- Residual — Root-mean-square difference between observations and model after parameter-fitting.

220

These data are provided as Climate and Forecasting (CF)-compliant NetCDF4 format, with the date of each time step and all parameter maps along with the latitude and longitude grid in annual files (DOI: 10.26179/5dd60df7469e2),. Data flags are provided in order to identify invalid pixels where there is insufficient data within the time period to accurately parameterise (less than 8 inputs). The coverage of the 1-day product is maximised due to the use of all three satellites, average percentage of invalid pixels remaining separated by latitude can be seen in Figure 4. These can be seen to increase with movement away from the poles due to the orbital geometry. For this parameterisation, as each satellite provides complete coverage every 5-days over the polar areas, the three combined require more than a day to ensure full coverage of the polar extremities. A compromise has been reached here, with the 1-day product covering the majority of the polar area and enabling a much product over many of the areas of interest. Recent drifting of Metop-A (in order to extend its lifetime) will lead to larger gaps in the 1-day product as the orbits become more similar between the satellites.

230

## 5 Dataset Applications

As presented in Table 1 of Fraser et al. (2014), the majority of previous studies using scatterometry in the cryosphere have applied a linear incidence angle parameterisation. Such studies would be repeatable using the B parameter provided here, in addition to those that feature the 4<sup>th</sup> order Fourier series azimuth characterisation. It can be seen therefore that these elements are widely used in ice sheet studies, as well as sea ice extent and type as seen in the OSI SAF product (Breivik et al., 2012). Figure 6 shows an application of this dataset in the form of an accurate ice edge product, comparable with that of OSI SAF (OSI SAF, 2019b). The algorithm presented here emulates that of OSI SAF by assuming the sea ice azimuthal anisotropy is low in comparison to that of open water. Figure 6a) shows a two-dimensional histogram of parameter fit residual (y-axis) vs

235



“maximum deviation” (x-axis). The maximum deviation metric is calculated as the maximum absolute deviation, in dB, of  
240 sigma0 as a function of azimuth, when using the 6 Fourier parameters presented in this dataset. Sea ice pixels have a low  
residual and low maximum deviation while ocean pixels have high residual and maximum deviation. Partitioning using one  
parameter alone cannot separate these classes, however combining these two parameters allows effective separation of the two  
surface types (here separated by the red line in Figure 6a). Figure 6b) shows the resulting ice edge (red line), as well as the  
OSI SAF ice edge (dotted orange line). Polynyas off Cape Darnley and the Ross Ice Shelf are visible along with a gap in the  
245 ice off Prydz bay, that is also visible in concentration data from the day (not shown). Further elucidation of this application is  
outside of the scope of this paper.

The data presented here are suitable for a wide array of cryosphere studies, including sea and glacial ice as is visible in Figure  
1 and Figure 2, with changes seen across the sea ice pack and in the varying geographic and climatological zones of the polar  
250 regions. These uses are shown by previous applications of the ASCAT sigma0 data. Here these data are taken a step further  
than the incidence angle parameterisations, additionally accounting for azimuth angle.. These data are provided on standard  
grids (NSIDC polar stereographic) in both hemispheres and across a variety of temporal resolutions in order to ensure full  
geographic coverage, using the sensors on-board all three MetOp satellites and taking advantage of the impressive coverage  
and consistency of the ASCAT dataset. We provide an extended time series of parameters covering 13 years in the case of the  
255 coarsest temporal resolution. The comparison of the three time steps seen in Figure 7 reveals that the longer averaging period  
of the 5-day product limits the sensitivity to shorter scale changes. The 5-day dataset therefore creates a less noisy dataset for  
point comparisons, and allows full use of the decadal timescale of the ASCAT instruments.

In the future we hope to be able to build and extend this dataset with the launch of the EUMETSAT polar system second  
generation (EPS-SG) MetOp -SG series, three satellites with proposed SCA scatterometers on-board due to launch in 2024  
260 (Lin et al., 2012), These aim to provide comparable measurements to ASCAT, but with a finer horizontal resolution and a  
wider swath (Lin et al., 2012).

## 6 Conclusion

Here we present a new dataset of scatterometry parameterisations taking advantage of the complete constellation of MetOp  
satellites in orbit. The use of three platforms (MetOp-A, -B and -C) allows multiple temporal resolutions of the product to be  
265 provided and full parameterisations achieved, accounting for both incidence and azimuth angle anisotropy. In this, the product  
is unique. It is hoped that this parameterisation, proven for cryosphere purposes (Fraser et al., 2014), will encourage the  
exploitation of scatterometry data for cryosphere science, research and monitoring. This dataset will be updated through the  
lifetime of the MetOp platforms, and will aim to be continued with the launch of the first of the MetOp-SG series in 2024.

## 7 Data Availability

270 The source data used for the derivation of these parameters is available from the EUMETSAT Data Centre  
(<http://www.eumetsat.int>), under Product "ASCAT GDS Level 1 Sigma0 resampled at 12.5 km Swath Grid — Metop", data  
code ASCSZR1B. The data presented in this paper are available from Australian Antarctic Data Centre, DOI:  
10.26179/5dd60df7469e2 (Fraser and Cartwright, 2021).

275 *Author Contributions:* ADF designed the processing, JC applied the processing to the data and packaged the dataset and JC  
and ADF wrote, edited and revised the paper. RPS assisted with comparisons between the NASA SCP product and the data  
presented here.

*Competing interests:* The authors declare that they have no conflict of interest.

*Disclaimer:* TEXT

280 *Acknowledgements:* Thanks to the EUMETSAT data centre for making the Level 1B data from ASCAT publicly available for  
processing, and fulfilling our considerable data requests. This work was supported by the Natural Environmental Research  
Council (grant NE/L002531/1). This project received grant funding from the Australian Government as part of the Antarctic  
Climate & Ecosystems Cooperative Research Centre, the Australian Research Council's Special Research Initiative for  
285 Antarctic Gateway Partnership (Project ID SR140300001) and the Antarctic Science Collaboration Initiative program (grant  
number ASCI000002). This work also contributes to Australian Antarctic Science Project 4301. Computation and storage  
facilities were provided by The National eResearch Collaboration Tools and Resources project (NeCTAR).

## Figures

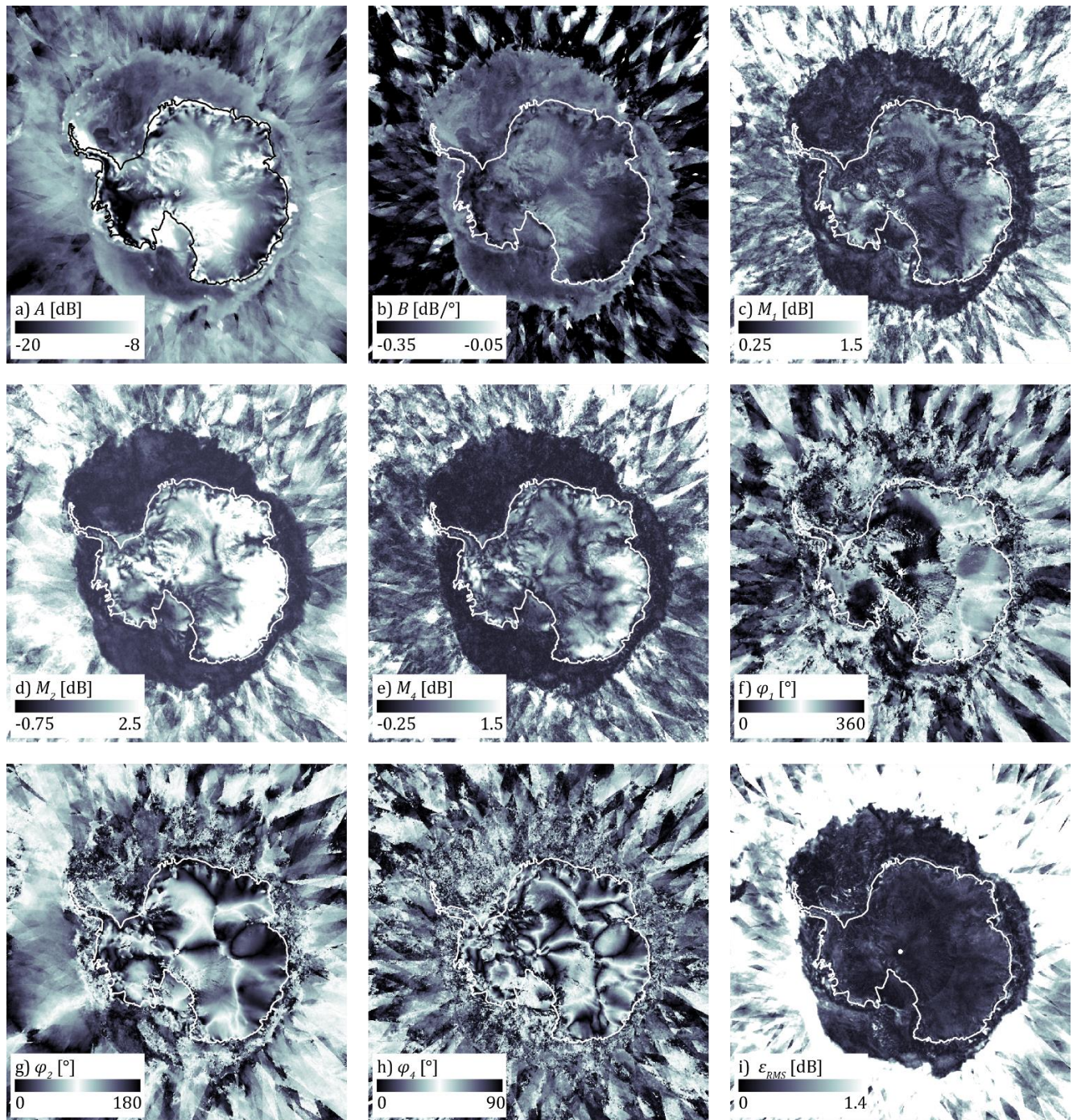


Figure 1: Example parameter maps at 2-day resolution over the Antarctica and the Southern Ocean, taken from 2017, day of year range 171–172 (20th – 21th April, 2017) using data from MetOp-A and -B. Coastlines outlined in black (a) or white (others, b) –i)).

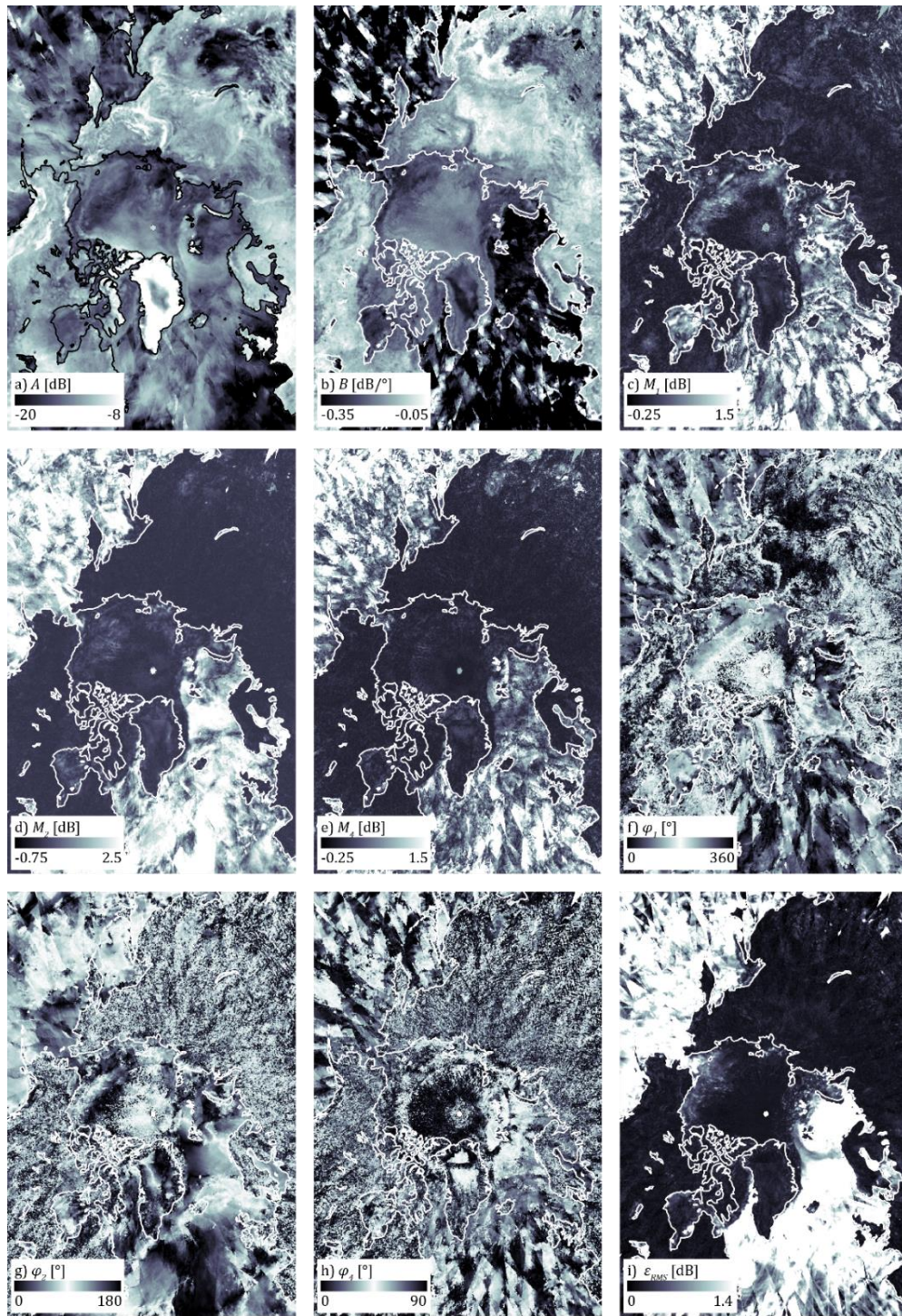
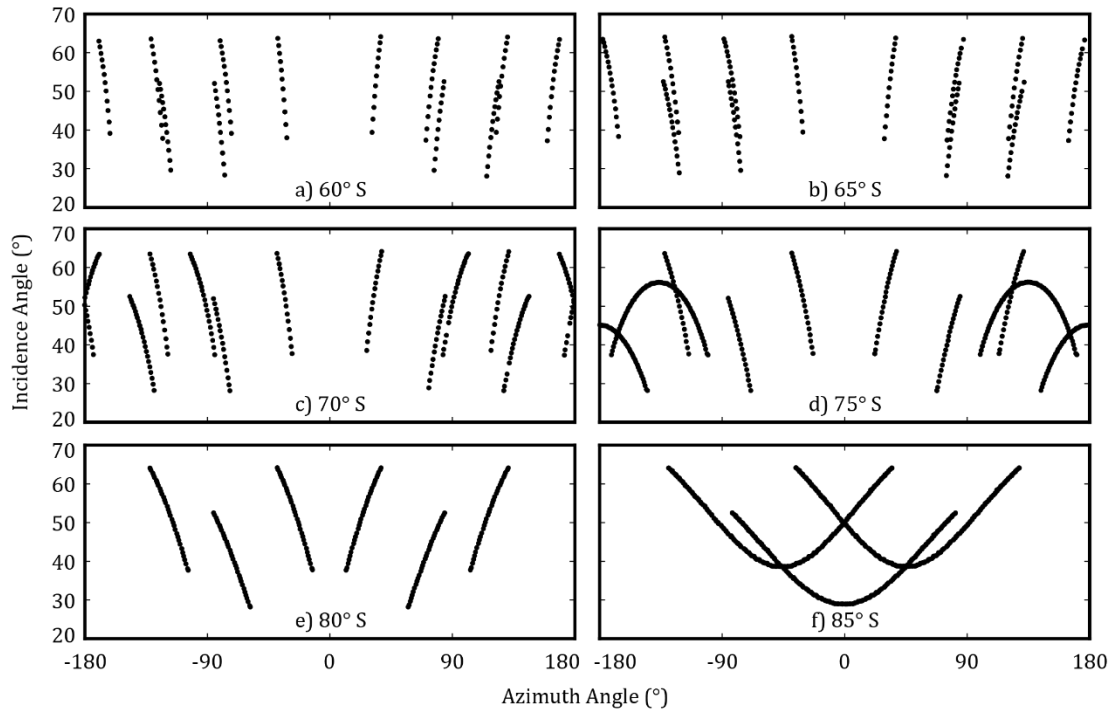
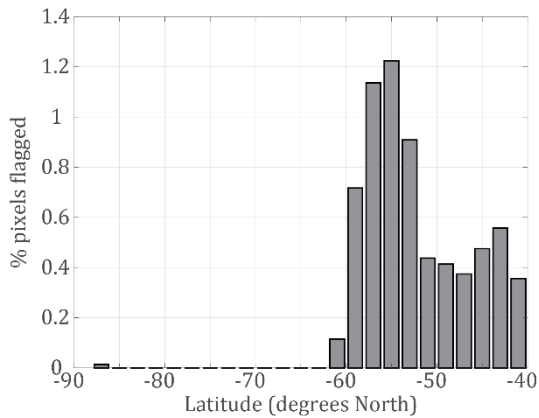


Figure 2: Example parameter maps at 2-day resolution over the Arctic, taken from 2017, day of year range 351–352 (21<sup>st</sup> – 22<sup>nd</sup> December, 2017) using data from MetOp-A and -B. Coastlines outlined in black (a) or white (b)–(i)).

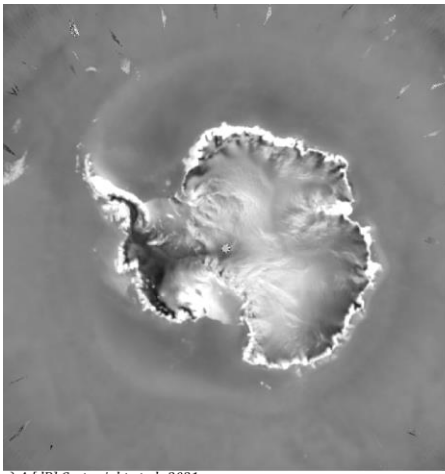


**Figure 3:** Plot of the azimuth and incidence angle distributions of the scatterometer swaths in the Southern Hemisphere as a function of latitude from a) 60 degrees to f) 85 degrees South from MetOp-B over June 2017.



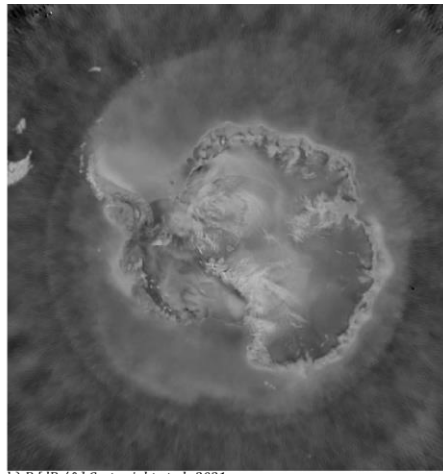
300

**Figure 4:** Invalid pixels binned by latitude as a percentage of total pixels in map for the data at 1-day resolution over the Southern Hemisphere (Metop-A, -B and -C). These patterns will be mirrored in the Northern hemisphere due to orbital geometry.



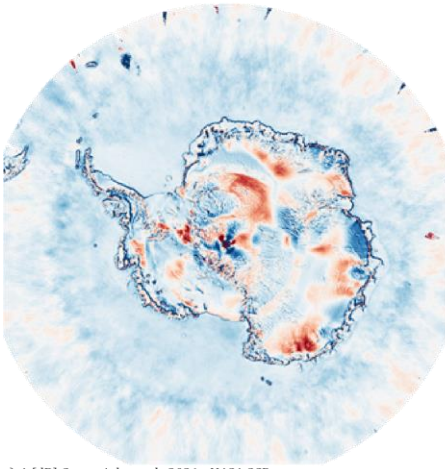
a) A [dB] Cartwright et al., 2021

-25 -5



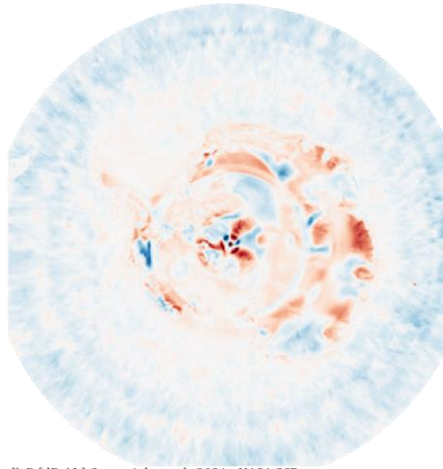
b) B [dB / °] Cartwright et al., 2021

-0.4 0



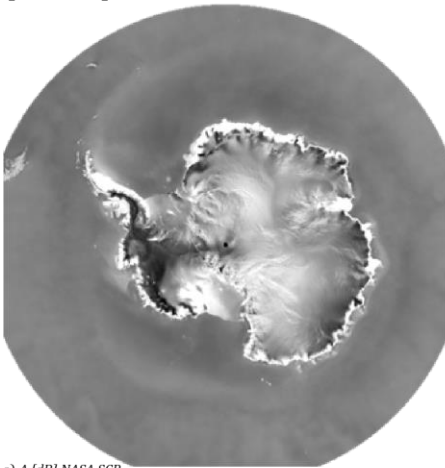
c) A [dB] Cartwright et al., 2021 - NASA SCP

-2 2



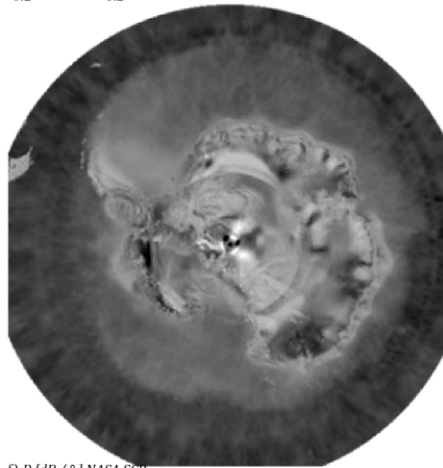
d) B [dB / °] Cartwright et al., 2021 - NASA SCP

-0.2 0.2



e) A [dB] NASA SCP

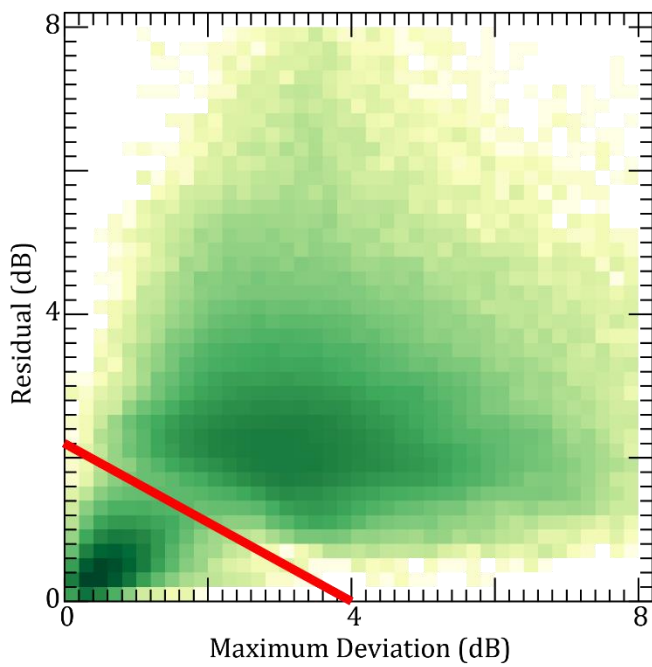
-25 -5



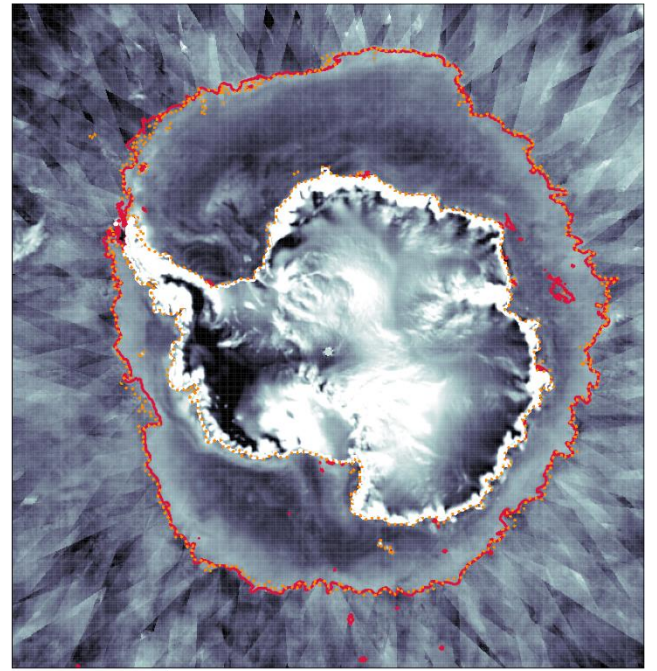
f) B [dB / °] NASA SCP

-0.4 0

305 **Figure 5: Comparison of NASA SCP product produced by BYU Remote Sensing facility and the dataset presented in this paper (without application of quality flags). Datasets are an average of 2017. The top row corresponds to the product presented here, Cartwright et al., 2021, the bottom row shows the NASA SCP product and the middle row the difference between the two. The left and right column are the A and B parameters respectively.**



a)



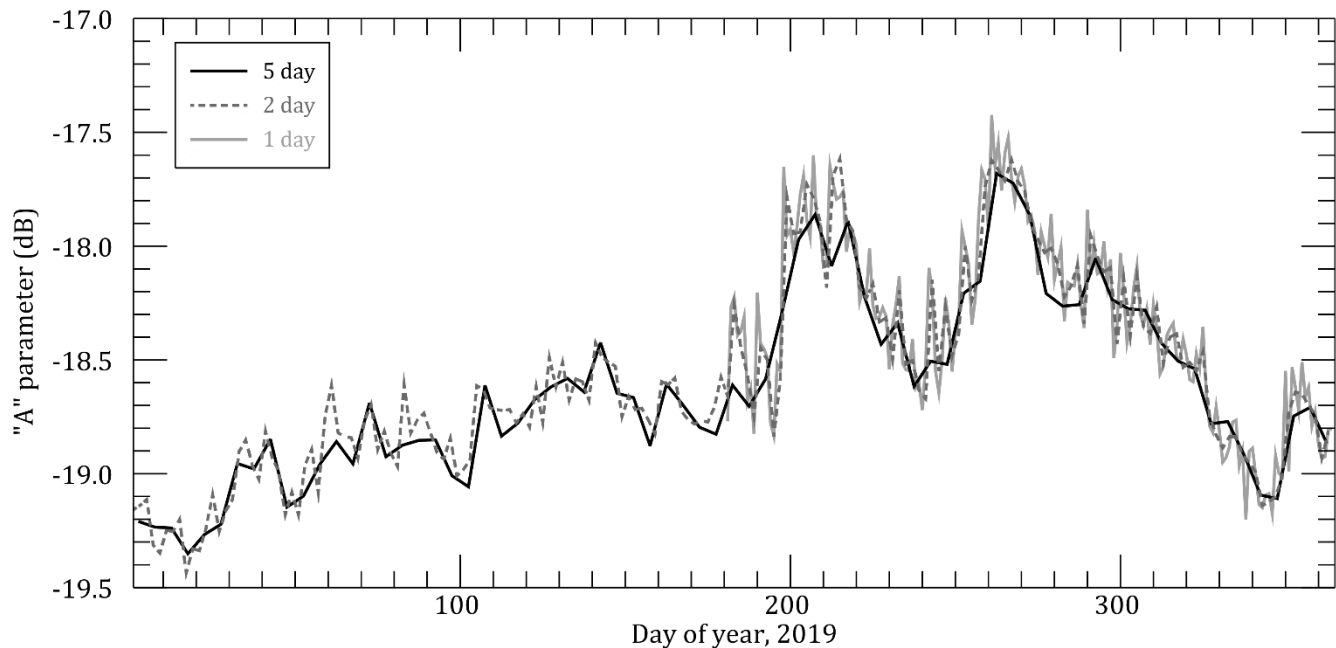
A [dB] ——— Cartwright et al., 2021 data thresholding

-20 — -8 ..... OSI SAF ice edge product

b)

310 **Figure 6: Application of dataset to surface type (sea ice vs open water) delineation. date shown is DOY 271-275, 2019 (28<sup>th</sup> September– 2<sup>nd</sup> October 2019. a) simple thresholding algorithm uses low azimuthal anisotropy over sea ice in comparison to high azimuthal anisotropy of sea water to classify the two surfaces, through parameters in the dataset. b) ‘A’ parameter map overlotted with ice edge from this dataset (red, solid) and that of OSISAF ice edge product (orange, dotted).**

-97.5614°E, -83.4303°N



315

**Figure 7: Comparisons of the A parameter in all three datasets, shown in decibels at a point in Antarctica for 2019. Black solid line denotes the 5-day dataset, grey dashed line the 2-day dataset and grey solid line the 1-day dataset.**

## References

- 320 Alley, K. E.: Studies of Antarctic Ice Shelf Stability: Surface Melting, Basal Melting, and Ice Flow Dynamics, Department of Geological Sciences, University of Colorado Boulder, 2017.  
Alley, K. E., Scambos, T. A., Miller, J. Z., Long, D. G., and MacFerrin, M.: Quantifying vulnerability of Antarctic ice shelves to hydrofracture using microwave scattering properties, *Remote Sensing of Environment*, 210, 297-306, 10.1016/j.rse.2018.03.025, 2018.
- 325 Ashcraft, I. S. and Long, D. G.: Comparison of methods for melt detection over Greenland using active and passive microwave measurements, *International Journal of Remote Sensing*, 27, 2469-2488, 10.1080/01431160500534465, 2007.  
Bartalis, Z., Scipal, K., and Wagner, W.: Azimuthal anisotropy of scatterometer measurements over land, *IEEE Transactions on Geoscience and Remote Sensing*, 44, 2083-2092, 10.1109/tgrs.2006.872084, 2006.
- 330 Bingham, A. W. and Drinkwater, M. R.: Recent changes in the microwave scattering properties of the Antarctic ice sheet, *IEEE Transactions on Geoscience and Remote Sensing*, 38, 1810-1820, 10.1109/36.851765, 2000.  
Bird, K. J., Charpentier, R. R., Gautier, D. L., Houseknecht, D. W., Klett, T. R., Pitman, J. K., Moore, T. E., Schenk, C. J., Tennyson, M. E., and Wandrey, C. R.: Circum-arctic resource appraisal: Estimates of undiscovered oil and gas north of the Arctic Circle, 10.3133/fs20083049, 2008.
- 335 Breivik, L.-A., Eastwood, S., and Lavergne, T.: Use of C-Band Scatterometer for Sea Ice Edge Identification, *IEEE Transactions on Geoscience and Remote Sensing*, 50, 2669-2677, 10.1109/tgrs.2012.2188898, 2012.  
Budge, J. S. and Long, D. G.: A Comprehensive Database for Antarctic Iceberg Tracking Using Scatterometer Data, *IEEE Journal of Selected Topics in Applied Earth Observations and Remote Sensing*, 11, 434-442, 10.1109/jstars.2017.2784186, 2018.



- Comiso, J. C., Cavalieri, D. J., and Markus, T.: Sea ice concentration, ice temperature, and snow depth using AMSR-E data, *IEEE Transactions on Geoscience and Remote Sensing*, 41, 243-252, 10.1109/TGRS.2002.808317, 2003.
- 340 Drinkwater, M. R., Long, D. G., and Bingham, A. W.: Greenland snow accumulation estimates from satellite radar scatterometer data, *Journal of Geophysical Research: Atmospheres*, 106, 33935-33950, 10.1029/2001jd900107, 2001.
- Figa-Saldaña, J., Wilson, J. J. W., Attema, E., Gelsthorpe, R., Drinkwater, M. R., and Stoffelen, A.: The advanced scatterometer (ASCAT) on the meteorological operational (MetOp) platform: A follow on for European wind scatterometers, *Canadian Journal of Remote Sensing*, 28, 404-412, 10.5589/m02-035, 2002.
- 345 Fraser, A. D. and Cartwright, J.: Advanced Scatterometer-derived Arctic and Antarctic backscatter anisotropy parameter maps (2), Australian Antarctic Data Centre [dataset], 10.26179/5dd60df7469e2, 2021.
- Fraser, A. D., Young, N. W., and Adams, N.: Comparison of Microwave Backscatter Anisotropy Parameterizations of the Antarctic Ice Sheet Using ASCAT, *IEEE Transactions on Geoscience and Remote Sensing*, 52, 1583-1595, 350 10.1109/tgrs.2013.2252621, 2014.
- Fraser, A. D., Nigro, M. A., Ligtenberg, S. R. M., Legresy, B., Inoue, M., Cassano, J. J., Kuipers Munneke, P., Lenaerts, J. T. M., Young, N. W., Treverrow, A., Van Den Broeke, M., and Enomoto, H.: Drivers of ASCAT C band backscatter variability in the dry snow zone of Antarctica, *Journal of Glaciology*, 62, 170-184, 10.1017/jog.2016.29, 2016.
- Holland, P. R., Bracegirdle, T. J., Dutrieux, P., Jenkins, A., and Steig, E. J.: West Antarctic ice loss influenced by internal climate variability and anthropogenic forcing, *Nature Geoscience*, 12, 718-724, 10.1038/s41561-019-0420-9, 2019.
- 355 Ledroit, M., Remy, F., and Minster, J. F.: Observations of the Antarctic ice sheet with the Seasat scatterometer: relation to katabatic-wind intensity and direction, *Journal of Glaciology*, 39, 385-396, 10.3189/s002214300001604x, 1993.
- Lin, C.-C., Betto, M., Belmonte Rivas, M., Stoffelen, A., and de Kloe, J.: EPS-SG Windscatterometer Concept Tradeoffs and Wind Retrieval Performance Assessment, *IEEE Transactions on Geoscience and Remote Sensing*, 50, 2458-2472, 360 10.1109/tgrs.2011.2180393, 2012.
- Long, D. G.: Polar Applications of Spaceborne Scatterometers, *IEEE J Sel Top Appl Earth Obs Remote Sens*, 10, 2307-2320, 10.1109/JSTARS.2016.2629418, 2017.
- Long, D. G. and Drinkwater, M. R.: Azimuth variation in microwave scatterometer and radiometer data over Antarctica, *IEEE Transactions on Geoscience and Remote Sensing*, 38, 1857-1870, 10.1109/36.851769, 2000.
- 365 Long, D. G., Hardin, P. J., and Whiting, P. T.: Resolution enhancement of spaceborne scatterometer data, *IEEE Transactions on Geoscience and Remote Sensing*, 31, 700-715, 10.1109/36.225536, 1993.
- Lubin, D. and Massom, R.: *Polar Remote Sensing: Volume I: Atmosphere and Oceans*, Springer Science & Business Media 2006.
- Massom, R. and Lubin, D.: *Polar Remote Sensing: Volume II: Ice Sheets*, Springer Praxis Books, Springer Berlin Heidelberg 2005.
- 370 Mätzler, C. and Hüppi, R.: Review of signature studies for microwave remote sensing of snowpacks, *Advances in Space Research*, 9, 253-265, 10.1016/0273-1177(89)90493-6, 1989.
- Müller, K., Sinisalo, A., Anschütz, H., Hamran, S.-E., Hagen, J.-O., McConnell, J. R., and Pasteris, D. R.: An 860 km surface mass-balance profile on the East Antarctic plateau derived by GPR, *Ann Glaciol*, 51, 1-8, 10.3189/172756410791392718, 375 2010.
- OSI SAF: Sea ice type product of the EUMETSAT Ocean and Sea Ice Satellite Application Facility, 2019a.
- OSI SAF: Sea ice edge product of the EUMETSAT Ocean and Sea Ice Satellite Application Facility, 2019b.
- Partington, K. and Flach, D.: *Synergetic Use of Remote Sensing Data in Ice Sheet Snow Accumulation and Topographic Change Estimates: Comparison of model output with available data*, Noveltis, Vexcel UK and Legos, 2003.
- 380 Pörtner, H., Roberts, D., Masson-Delmotte, V., Zhai, P., Tignor, M., Poloczanska, E., Mintenbeck, K., Nicolai, M., Okem, A., and Petzold, J.: *IPCC Special Report on the Ocean and Cryosphere in a Changing Climate*, IPCC Intergovernmental Panel on Climate Change: Geneva, Switzerland, 2019.
- Remy, F., Ledroit, M., and Minster, J. F.: Katabatic wind intensity and direction over Antarctica derived from scatterometer data, *Geophysical Research Letters*, 19, 1021-1024, 10.1029/92gl00970, 1992.
- 385 Rignot, E., Echelmeyer, K., and Krabill, W.: Penetration depth of interferometric synthetic-aperture radar signals in snow and ice, *Geophysical Research Letters*, 28, 3501-3504, 10.1029/2000gl012484, 2001.
- Rott, H., Sturm, K., and Miller, H.: Active and passive microwave signatures of Antarctic firn by means of field measurements and satellite data, *Ann Glaciol*, 17, 337-343, 10.3189/S0260305500013070, 1993.

- 390 Shepherd, A., Ivins, E., Rignot, E., Smith, B., van den Broeke, M., Velicogna, I., Whitehouse, P., Briggs, K., Joughin, I., Krinner, G., Nowicki, S., Payne, T., Scambos, T., Schlegel, N., A. G., Agosta, C., Ahlstrøm, A., Babonis, G., Barletta, V. R., Bjørk, A. A., Blazquez, A., Bonin, J., Colgan, W., Csatho, B., Cullather, R., Engdahl, M. E., Felikson, D., Fettweis, X., Forsberg, R., Hogg, A. E., Gallee, H., Gardner, A., Gilbert, L., Gourmelen, N., Groh, A., Gunter, B., Hanna, E., Harig, C., Helm, V., Horvath, A., Horwath, M., Khan, S., Kjeldsen, K. K., Konrad, H., Langen, P. L., Lecavalier, B., Loomis, B., Luthcke, S., McMillan, M., Melini, D., Mernild, S., Mohajerani, Y., Moore, P., Mottram, R., Mouginot, J., Moyano, G., Muir, A.,
- 395 Nagler, T., Nield, G., Nilsson, J., Noël, B., Otsuka, I., Pattle, M. E., Peltier, W. R., Pie, N., Rietbroek, R., Rott, H., Sandberg Sørensen, L., Sasgen, I., Save, H., Scheuchl, B., Schrama, E., Schröder, L., Seo, K.-W., Simonsen, S. B., Slater, T., Spada, G., Sutterley, T., Talpe, M., Tarasov, L., van de Berg, W. J., van der Wal, W., van Wessem, M., Vishwakarma, B. D., Wiese, D., Wilton, D., Wagner, T., Wouters, B., Wuite, J., and The, I. T.: Mass balance of the Greenland Ice Sheet from 1992 to 2018, *Nature*, 579, 233-239, 10.1038/s41586-019-1855-2, 2020.
- 400 Spencer, M. W., Chialin, W., and Long, D. G.: Tradeoffs in the design of a spaceborne scanning pencil beam scatterometer: application to SeaWinds, *IEEE Transactions on Geoscience and Remote Sensing*, 35, 115-126, 10.1109/36.551940, 1997.
- Stroeve, J. C., Serreze, M. C., Holland, M. M., Kay, J. E., Malanik, J., and Barrett, A. P.: The Arctic's rapidly shrinking sea ice cover: a research synthesis, *Climatic Change*, 110, 1005-1027, 10.1007/s10584-011-0101-1, 2011.
- 405 Trusel, L. D., Frey, K. E., and Das, S. B.: Antarctic surface melting dynamics: Enhanced perspectives from radar scatterometer data, *Journal of Geophysical Research: Earth Surface*, 117, 10.1029/2011JF002126, 2012.
- Ulaby, F. T., Siquera, P., Nashashibi, A., and Sarabandi, K.: Semi-empirical model for radar backscatter from snow at 35 and 95 GHz, *IEEE Transactions on Geoscience and Remote Sensing*, 34, 1059-1065, 10.1109/36.536521, 1996.
- Vogelzang, J. and Stoffelen, A.: ASCAT Ultrahigh-Resolution Wind Products on Optimized Grids, *IEEE Journal of Selected Topics in Applied Earth Observations and Remote Sensing*, 10, 2332-2339, 10.1109/jstars.2016.2623861, 2017.
- 410 Young, N. W. and Hyland, G.: Applications of time series of microwave backscatter over the Antarctic region, *Third ERS Symposium on Space at the service of our Environment*, Florence, Italy, 1997, 1007, 1997.
- Yurchak, B.: Some Features of the Volume Component of Radar Backscatter from Thick and Dry Snow Cover, in: *Advances in Geoscience and Remote Sensing*, edited by: Jedlovec, G., Intech, Rijeka, Croatia, 10.5772/8339, 2009.